Achieving High-Performance Room-Temperature Sodium–Sulfur Batteries With S@Interconnected Mesoporous Carbon Hollow Nanospheres

Yun-Xiao Wang,[†] Jianping Yang,[‡] Weihong Lai,[†] Shu-Lei Chou,*,[†] Qin-Fen Gu,[§] Hua Kun Liu,[†] Dongyuan Zhao,[‡] and Shi Xue Dou[†]

[†]Institute for Superconducting & Electronic Materials, Australian Institute of Innovative Materials, University of Wollongong, Innovation Campus, Squires Way, North Wollongong, New South Wales 2500, Australia

[‡]Department of Chemical Engineering, Monash University, Clayton, Victoria 3800, Australia

[§]Australian Synchrotron, 800 Blackburn Road, Clayton, Victoria 3168, Australia

S *Supporting Information*

ABSTRACT: Despite the high theoretical capacity of the sodium–sulfur battery, its application is seriously restrained by the challenges due to its low sulfur electroactivity and accelerated shuttle effect, which lead to low accessible capacity and fast decay. Herein, an elaborate carbon framework, interconnected mesoporous hollow carbon nanospheres, is reported as an effective sulfur host to achieve excellent electrochemical performance. Based on *in situ* synchrotron X-ray diffraction, the mechanism of the room temperature Na/S battery is proposed to be reversible reactions between S_8 and Na_2S_4, corresponding to a theoretical capacity of 418 mAh g^{-1}. The cell is capable of achieving high capacity retention of ~88.8% over 200 cycles, and superior rate capability with reversible capacity of ~390 and 127 mAh g^{-1} at 0.1 and 5 A g^{-1}, respectively.

Room-temperature sodium–sulfur (RT-Na/S) batteries are triggering tremendous research interest as candidates to power our future society, especially in conjunction with sustainable energy sources.[1−4] The theoretical capacity of a Na/S battery is as high as 1672 mAh g^{-1} (based on the formation of Na_2S). This system also exhibits overwhelming advantages in terms of low cost, resource abundance, and environmental benignity. Nevertheless, the operation of a Na/S battery at ambient temperature suffers from low reversible capacity and extremely fast capacity fade during cycling.[5−7] Its low reversible capacity is due to the low conductivity of sulfur and the slow reaction kinetics between S and Na. In addition, the shuttle effect of polysulfides is highly exacerbated in the RT-Na/S system, resulting in a low Coulombic efficiency and rapid capacity decay during cycling. Manthiram's group has made great efforts toward the enhancement of RT-Na/S batteries, including fabricating a class of sodium polysulfides,[8] introducing carbonaceous interlayers,[9] exploiting Na_2S cathodes, and utilizing carbon-coated Nafion separator.[10] These strategies, however, tend to result in complicated synthetic processes, decreased theoretical capacity, and extra cost. Consistent efforts have been made to seek highly efficient S-hosts, including Ketjenblack,[11] Cu-decorated mesoporous carbon,[12] microporous carbon,[13] hollow

carbon spheres,[14] and C nanofibers.[15] Most recently, Archer et al.[16] reported that their microporous carbon polyhedron sulfur composite (MCPS) cathode could achieve superior electrochemical performance via lowering the S loading ratio (47%) and utilizing costly ionic liquid electrolyte. It is notable, however, that this type of cathode suffers from rapid capacity decay to ~300 mAh g^{-1} over only 10 cycles when higher S loading (63%) and a conventional carbonate electrolyte is applied. Developing high-loading S cathode with an effective S-host is the most essential and practical target for the further optimization and large-scale application of RT-Na/S batteries. Moreover, it is extremely challenging to observe the reaction processes and understand the Na-storage mechanism of S. This is because both sodium metal and sodium polysulfides are extremely sensitive to air, and the *in situ* characterization platforms that can track the liquid-phase polysulfide intermediates are not widely well-established as yet. Furthermore, the charge/discharge products of RT-Na/S batteries are difficult to detect and capture.

Herein, inspired by the nanostructural configuration of sulfur cathode in lithium–sulfur batteries,[17−31] we propose interconnected mesoporous carbon hollow nanospheres (*i*MCHS) as an effective matrix for sulfur loading. First, the C backbone is continuous and interlaced, which ensures high tap density, high structural intimacy, and the integrity of the nanocomposite after S loading. Second, the inner hollow nanospaces can encapsulate a high sulfur ratio and tolerate the volume changes of the interior sulfur. The outer carbon nanoshells can confine the polysulfides that are formed, thereby inhibiting the shuttle effect. On the other hand, the mesoporous carbon shells can not only serve as a highly conductive network for S and electron transport, but also supply open active diffusion channels. Moreover, the carbon mesopores can embed a certain amount of sulfur and localize the diffluent polysulfides. Significantly, the cell could deliver high reversible capacity of 340 and 292 mAh g^{-1} after 100 and 200 cycles, and outstanding rate capability of ~390 and 127 mAh g^{-1} at 0.1 and 5 A g^{-1}, respectively. Furthermore, a reversible reaction mechanism between S_8 and Na_2S_4 has been first confirmed via *in situ* synchrotron XRD for the room-temperature
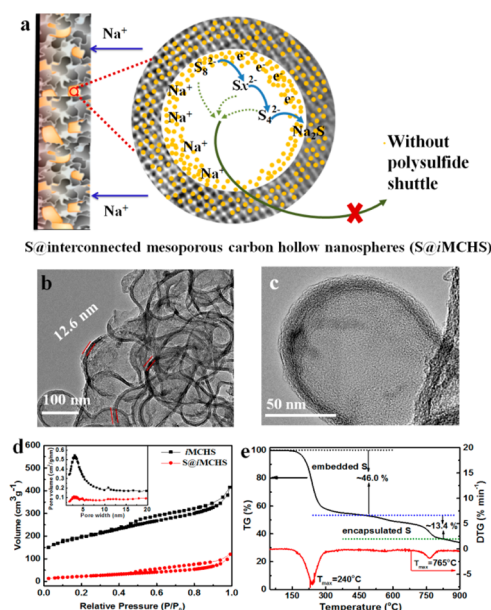
Figure 1. (a) Schematic of the confinement in the S@*i*MCHS nanocomposite. TEM images at (b) low and (c) high resolution of S@*i*MCHS nanocomposite. (d) N$_2$ absorption/desorption isotherms and pore size distribution (inset) for the pure *i*MCHS matrix and S@*i*MCHS nanocomposite. (e) Thermogravimetry (TG) and derivative thermogravimetry (DTG) curves of S@*i*MCHS nanocomposite.

sodium–sulfur batteries. Thus, a successful S incorporated *i*MCHS nanocomposite (S@*i*MCHS) is able to exhibit high sodium electroactivity and enhanced kinetics, holding great promise for achieving high-performance RT-Na/S batteries.

As shown in Figure 1a, a large amount of sulfur could be encapsulated in the hollow spaces and embedded in the mesopores of the *i*MCHS matrix via the facile melt-diffusion method, for which the *i*MCHS matrix was fabricated by modifying our previous method (Supporting Information, Figure S1).[32] Compared to the pure *i*MCHS (Supporting Information, Figure S2), the S@*i*MCHS nanocomposite shows low transparency (Figure S3), indicating the successful loading of S. Furthermore, the surface of S@*i*MCHS is rough (Figure S3b), with small nanoparticles dotted on the surface, implying S embedding in the mesopores. Transmission electron microscopy (TEM) (Figure 1b) demonstrates that the frameworks of S@*i*MCHS are interconnected with an average wall thickness of ~12.6 nm, which is thicker than pure *i*MCHS (~10 nm, Figure S3d), indicating the interior accumulation of S along the carbon shell. Moreover, numerous mesopores can be observed in the carbon walls (Figure 1c). The elemental mappings shown in Figures S3c confirm the uniform dispersion of S in the *i*MCHS matrix, with S encapsulated in the inner hollow spaces and embedded in the mesopores. The N$_2$ absorption analysis of *i*MCHS and the S@*i*MCHS hybrids shows type-IV curves with a gradual capillary condensation step in the relative pressure range of 0.5–0.8 (Figure 1d), suggesting the presence of hierarchical mesoporous structures. As revealed by the pore size distribution (inset), uniform mesopore diameters centered at 3.6–3.8 nm can be observed. For the *i*MCHS host, the Brunauer–Emmett–Teller (BET) surface area and total pore volume are calculated to be as high as 663 m^2 g^{-1} and 0.64 cm^3 g^{-1}, respectively. The corresponding values for the S@*i*MCHS hybrid decrease to 85.5 m^2 g^{-1} and 0.18 cm^3 g^{-1}, respectively, which is due to the occupation of S in both the hollow spaces and the mesopores of
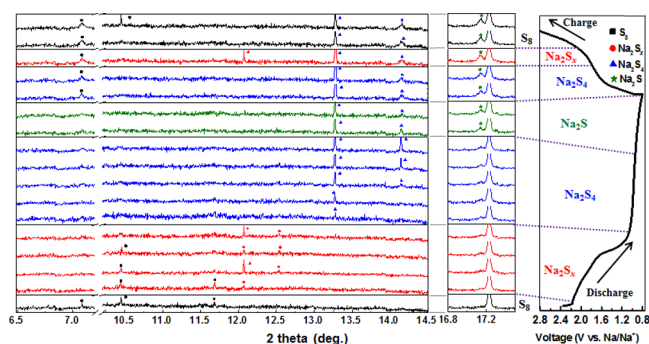

Figure 2. *In situ* synchrotron XRD patterns of the RT-Na/S@*i*MCHS cells (left) with the initial galvanostatic charge/discharge curve (right).

the *i*MCHS host. The pore volume variation of 0.457 cm^3 g^{-1} corresponds to a maximum of 0.946 g of S embedded in the mesopores for each gram of *i*MCHS (embedded S), which is consistent with the TGA results (S ratio of ~46%, Figure 1e) with the maximum weight loss rate (T_{max}) occurred at 240 °C. In contrast, the remaining 13.4% of the S could realize sublimation at high temperature, with T_{max} of 765 °C, which is because this portion of the S is encapsulated in the inner hollow spaces (encapsulated S) and hard to evaporate. It is postulated that the embedded S shows high electroactivity due to the intimate contact between the carbon matrix and the S nanoparticles.[19,21] The encapsulated S could be fully enclosed in the hollow void spaces, thereby preventing the polysulfides from dissolving into the electrolyte and accommodating the volume expansion during discharge/charge processes.[22,26−28] X-ray diffraction (XRD) and the Raman spectroscopy further indicate the complete incorporation of S into the *i*MCHS host (Figure S4)

To understand the Na−S chemistry, *in situ* synchrotron XRD data (λ = 0.6888 Å) were collected via the Powder Diffraction Beamline at the Australian Synchrotron, which could track the oxidation-state changes of S species during discharge/charge processes. A three-dimensional (3D) line plot of the various oxidation states of S during the first cycle is presented in Figure 2. Owing to the high resolution of synchrotron XRD, three conspicuous peaks at 7.08°, 10.44°, and 11.68° for the fresh cell can be observed and indexed to the (113), (222), and (026) planes of S$_8$ (JCPDF no. 77-0145). When the S@*i*MCHS cathode is discharged from 2.3 to 1.6 V, the three peaks of S$_8$ gradually disappear, confirming the reduction of S$_8$ species and rings broken; two new peaks evolve at 12.06° and 12.54°, which can be assigned to the formation of higher polysulfide species (Na$_2$S$_x$, $5 \leq x \leq 8$). When further discharged to 1.0 V, two new peaks are generated at 13.27° and 14.15°, which can be ascribed to the formation of Na$_2$S$_4$, corresponding to the (213) and (312) planes of Na$_2$S$_4$ (JCPDF no. 71-0516), respectively. From 1.0 to 0.8 V, the peak intensity of Na$_2$S$_4$ is weakened, and a new diffraction peak at 17.14° is developed, which can be indexed as the (220) peak of Na$_2$S (JCPDF no. 77-2149). When the cell is charged back to 2.8 V, the process corresponds to the oxidation of polysulfides to the neutral elemental S$_8$, in which the presence of Na$_2$S$_4$, Na$_2$S$_x$, and S$_8$ is detectable. Meanwhile, it is noteworthy that the (220) diffraction peak of Na$_2$S is accumulated without reduction into long-chain polysulfides, indicating the irreversibility of Na$_2$S.

The sodiation/desodiation behavior of the S@*i*MCHS was investigated in 2032 coin-type cells. When paired with Na anode, the S@*i*MCHS cathode loading mass was 3.2−4.1 mg cm^{-2}, and the optimized electrolyte of 1.0 M NaClO$_4$ in propylene
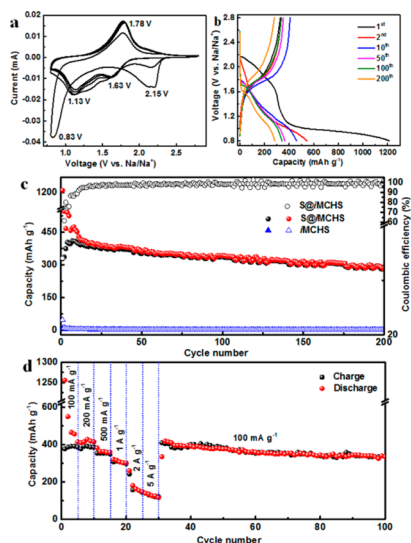
Figure 3. (a) Cyclic voltammograms for the initial five cycles, and (b) galvanostatic charge/discharge profiles for selected cycles of RT-Na/S@iMCHS cells. (c) Cycling performance of S@iMCHS and iMCHS electrodes at 100 mA g^{-1}. (d) Rate capability at various current densities of the RT-Na/S@iMCHS cell.

carbonate/ethylene carbonate in a volume ratio of 1:1 with 5 wt % fluoroethylene carbonate additive (PC/EC + 5 wt % FEC) was applied for all cells. As revealed via the cyclic voltammograms (CVs) in Figure 3a, the RT-Na/S@iMCHS cell shows two prominent peaks centered at around 2.15 and 0.83 V during the initial cathodic scan. The high-voltage peak (2.15 V) corresponds to the solid−liquid transition from elemental sulfur to dissolved long-chain polysulfides. During the subsequent cathodic sweep (2.15−0.83 V), the soluble high-order polysulfides are further sodiated to less soluble Na_2S_4. The low-voltage peak (0.83 V) is likely to be attributable to the formation of Na_2S via sodiation of the chemically bonded S.[8−10,33] In the following cathodic sweep, two strong cathodic peaks at 1.63 and 1.13 V are evolved and are highly repeatable. According to the formation voltage of polysulfides from in situ synchrotron XRD, the peak at 1.63 V should be ascribed to the reaction leading to Na_2S_x formation (5 ≤ x ≤ 8); the low-voltage peak (1.13 V) corresponds to the formation of Na_2S_4. For the anodic scan, only one repeatable peak at 1.78 V (vs Na/Na$^+$) is observed over all the cycles, corresponding to the oxidation of short-chain sodium sulfides into long-chain polysulfides. The high repeatability of the CV curves demonstrates the good cycling stability of the S@iMCHS cathode. Figure 3b shows the discharge/charge profiles of the 1st, 2nd, 10th, 50th, 100th, and 200th cycles at 100 mA g^{-1}. Consistent with the CV curves, a sloping plateau arises from 2.2 to 1.65 V, and a long plateau occurs in the range of 1.0 to 0.8 V during the first discharge process. The initial discharge capacity is as high as 1215 mAh g^{-1}, which indicates the high utilization and activity of S in the cathode. It is notable that the low-voltage plateau is irreversible. The cell delivers a low reversible capacity of ∼328 mAh g^{-1}, indicating that the thus-formed solid Na_2S could not be reversibly oxidized, but was nonuniformly deposited on the cathode. As the cycling proceeded over 200 cycles, the accumulated nonconductive Na_2S deposition would reduce the charge transfer rate and block ion accessibility, leading to slow kinetics and serious polarization, which is responsible for the gradual capacity fade and increased charge/discharge potential difference. Interestingly, even though the conductivity of the cell

is gradually decreased, the discharge/charge plateaus are distinct and repeated over 200 cycles, indicating the high electrochemical activity and good cycling stability of the RT-Na/S@iMCHS cell. This cycling stability of the S@iMCHS cathode is displayed in Figure 3c at a current density of 100 mA g^{-1} over 200 cycles. High charge capacity retention of ∼88.8% (∼292 mAh g^{-1}) is achieved after 200 cycles, implying that the dissolution of long-chain polysulfides is decelerated via the confinement in the elaborate iMCHS host, thereby maintaining stable specific capacity and cycling performance. Additionally, the capacity contribution of iMCHS is negligible during the applied voltage range (0.8−2.8 V). Moreover, the RT-Na/S@iMCHS cell delivers reversible capacities of ∼391, 386, 352, 305, 174, and 127 mAh g^{-1} at 0.1, 0.2, 0.5, 1, 2, and 5 A g^{-1}, respectively, demonstrating excellent rate capacity (Figure 3d). Impressively, the reversible capacity can be recovered to 335 mAh g^{-1} over 100 cycles when the applied current is reversed back to 100 mA g^{-1}. Furthermore, the discharge/charge curves of the S@iMCHS composite show distinct sodiation/desodiation plateaus at 0.1, 0.2, 0.5, 1, and 2 A g^{-1} (Figure S5), further proving the high electroactivity of S and the fast electron diffusion rate with the aid of the iMCHS frameworks.[12,17,19,21,24,34] The superiority of enclosed iMCHS frameworks is highlighted in stark contrast to the open matrixes, including mesoporous carbon and reduced graphene oxides (RGO). The corresponding S@mesoporous and S@RGO are proven to be inactive (Figure S6). It is also noteworthy that self-discharge occurs, because the active materials gradually dissolve and shuttle to the sodium anode. They then react with sodium metal, followed by conversion into high-order polysulfides, which, in turn, leads to a decrease in the open-circuit voltage and discharge capacity. Even though the iMCHS matrix is capable of trapping S, serious self-discharge behavior is an inevitable phenomenon in the Na/S cell, and high-order polysulfides continue to dissolve slowly in the electrolyte, even during the resting state. As shown in Figure S7, the rest time of cells is a critical parameter for achieving restrained self-discharge behavior and satisfactory electrochemical performance. It is clear that resting the cell for 2 h would deliver distinct charge/discharge plateaus and the highest reversible capacity.

Furthermore, the S@iMCHS electrodes before and after rate-capability testing were investigated via scanning electron microscopy (SEM) and TEM. At a low magnification (Figure S8a,c), the electrodes before and after cycling do not show any distinct change in the morphology, but only show more slight cracking on the surface of the electrode after cycling. Significantly, compared to the fresh electrode at high magnification (Figure S8b), a large amount of low conductive substance is deposited on the carbon skeleton (Figure S8d), which can be attributed to the Na_2S accumulation and solid electrolyte interphase (SEI) film formation during cycling. This speculation is further confirmed by the element mapping images (Figure S9a), showing coincident signals of the elements Na, S, and C. The strong signals of the elements Na, O, and F could prove the existence of an SEI film.[35] The corresponding phase mapping images (Figure S9b) verify the coexistence of NaF, Na_2O, and Na_2S. In addition, as evidenced by impedance spectroscopy at selected cycles, the conspicuous resistance increase over cycling can imply the accumulation of low-conductivity Na_2S and SEI film formation (Figure S10). By contrast with the reported results (Table S1), this work achieves significant enhancements on cycling stability, capacity retention, and rate capability. Based on the above results and analyses, the electrochemical reaction of RT-Na/S@iMCHS mainly origi-

nates from the reversible conversion between long-chain Na_2S_x ($5 \leq x \leq 8$) and short-chain Na_2S_4, corresponding to a theoretical capacity of 418.75 mAh g^{-1}. This explains why the RT-Na/S@*i*MCHS can only reach a reversible capacity of 410 mAh g^{-1} at the most. In addition, as cycling proceeds, this mechanism would allow more and more nonconductive Na_2S to accumulate on the cathode surface, leading to an increase in the cell internal resistance and continuous gradual capacity decay, which is in good agreement with the electrochemical performance in Figure 3.

In summary, the accessible capacity and cycling stability of the RT-Na/S batteries are significantly enhanced via exploiting hollow mesoporous carbon nanospheres as an effective matrix. The abundant mesopores of the carbon shells serve as minicontainers to embed intimately the S loading, which could greatly improve the overall conductivity of the S cathode, leading to high active material utilization and S electroactivity. Thus, the highest reversible capacity (410 mAh g^{-1}) can reach the theoretical capacity (418 mAh g^{-1}). Meanwhile, the embedded S would be localized due to the confinement in the mesopores, which could inhibit the shuttle phenomenon of the polysulfides that are formed during cycling. On the other hand, the nanostructured carbon shells can encapsulate sodium-polysulfide species inside the mesopores and hollow spaces, thereby suppressing the polysulfide shuttle to the anode and thus maintaining sustainable capacity of 292 mAh g^{-1} over 200 cycles. This elaborate *i*MCHS host, therefore, is capable of enhancing the electrochemical activity of S, suppressing the severe shuttle effect, and preserving the material morphology and electrode integrity. The CV curves, charge/discharge profiles, and *in situ* synchrotron XRD patterns of RT-Na/S@*i*MCHS have been combined to reveal that the sodiation process originates from a class of sodium polysufide intermediates, ranging from possible Na_2S_x ($x = 8, 6$, and 5) to Na_2S_4, and then to Na_2S, whereas the desodiation process corresponds to the reversible reductions from Na_2S_4 to S_8. The favorable nanostructure and our investigation of the mechanisms will shine a light on future optimization of RT-Na/S batteries.

ASSOCIATED CONTENT

Ⓢ Supporting Information

The Supporting Information is available free of charge on the ACS Publications website at DOI: 10.1021/jacs.6b08685.

Experimental details (PDF)

AUTHOR INFORMATION

Corresponding Author
*shulei@uow.edu.au

ORCID Ⓞ
Jianping Yang: 0000-0003-1495-270X
Shu-Lei Chou: 0000-0003-1155-6082

Notes
The authors declare no competing financial interest.

ACKNOWLEDGMENTS

REFERENCES

(1) Yabuuchi, N.; Kubota, K.; Dahbi, M.; Komaba, S. *Chem. Rev.* **2014**, *114*, 11636.
(2) Dunn, B.; Kamath, H.; Tarascon, J.-M. *Science* **2011**, *334*, 928.
(3) Adelhelm, P.; Hartmann, P.; Bender, C. L.; Busche, M.; Eufinger, C.; Janek, J. *Beilstein J. Nanotechnol.* **2015**, *6*, 1016.
(4) Kim, S. W.; Seo, D. H.; Ma, X.; Ceder, G.; Kang, K. *Adv. Energy Mater.* **2012**, *2*, 710.
(5) Ryu, H.; Kim, T.; Kim, K.; Ahn, J.-H.; Nam, T.; Wang, G.; Ahn, H.-J. *J. Power Sources* **2011**, *196*, 5186.
(6) Hueso, K. B.; Armand, M.; Rojo, T. *Energy Environ. Sci.* **2013**, *6*, 734.
(7) Seh, Z. W.; Sun, J.; Sun, Y.; Cui, Y. *ACS Cent. Sci.* **2015**, *1*, 449.
(8) Yu, X. W.; Manthiram, A. *J. Phys. Chem. Lett.* **2014**, *5*, 1943.
(9) Yu, X. W.; Manthiram, A. *ChemElectroChem* **2014**, *1*, 1275.
(10) Yu, X. W.; Manthiram, A. *Chem. Mater.* **2016**, *28*, 896.
(11) Kohl, M.; Borrmann, F.; Althues, H.; Kaskel, S. *Adv. Energy Mater.* **2016**, *6*, 1502185.
(12) Zheng, S.; Han, P.; Han, Z.; Li, P.; Zhang, H.; Yang, J. *Adv. Energy Mater.* **2014**, *4*, 1400226.
(13) Xin, S.; Yin, Y.-X.; Guo, Y.-G.; Wan, L.-J. *Adv. Mater.* **2014**, *26*, 1261.
(14) Lee, D.-J.; Park, J.-W.; Hasa, I.; Sun, Y.-K.; Scrosati, B.; Hassoun, J. *J. Mater. Chem. A* **2013**, *1*, 5256.
(15) Hwang, T. H.; Jung, D. S.; Kim, J.-S.; Kim, B. G.; Choi, J. W. *Nano Lett.* **2013**, *13*, 4532.
(16) Wei, S.; Xu, S.; Agrawral, A.; Choudhury, S.; Lu, Y.; Tu, Z.; Ma, L.; Archer, L. A. *Nat. Commun.* **2016**, *7*, 11722.
(17) Ji, X.; Lee, K. T.; Nazar, L. F. *Nat. Mater.* **2009**, *8*, 500.
(18) Zhang, B.; Qin, X.; Li, G. R.; Gao, X. P. *Energy Environ. Sci.* **2010**, *3*, 1531.
(19) Chen, S. R.; Zhai, Y. P.; Xu, G. L.; Jiang, Y. X.; Zhao, D. Y.; Li, J. T.; Huang, L.; Sun, S. G. *Electrochim. Acta* **2011**, *56*, 9549.
(20) Ji, L.; Rao, M.; Zheng, H.; Zhang, L.; Li, Y.; Duan, W.; Guo, J.; Cairns, E. J.; Zhang, Y. *J. Am. Chem. Soc.* **2011**, *133*, 18522.
(21) Schuster, J.; He, G.; Mandlmeier, B.; Yim, T.; Lee, K. T.; Bein, T.; Nazar, L. F. *Angew. Chem., Int. Ed.* **2012**, *51*, 3591.
(22) Li, W. Y.; Zheng, G. Y.; Yang, Y.; Seh, Z. W.; Liu, N.; Cui, Y. *Proc. Natl. Acad. Sci. U. S. A.* **2013**, *110*, 7148.
(23) Chen, R. J.; Zhao, T.; Lu, J.; Wu, F.; Li, L.; Chen, J. Z.; Tan, G. Q.; Ye, Y. S.; Amine, K. *Nano Lett.* **2013**, *13*, 4642.
(24) Zhang, W. H.; Qiao, D.; Pan, J. X.; Cao, Y. L.; Yang, H. X.; Ai, X. P. *Electrochim. Acta* **2013**, *87*, 497.
(25) Wang, C.; Wan, W.; Chen, J.-T.; Zhou, H.-H.; Zhang, X.-X.; Yuan, L.-X.; Huang, Y.-H. *J. Mater. Chem. A* **2013**, *1*, 1716.
(26) Zhang, K.; Zhao, Q.; Tao, Z.; Chen, J. *Nano Res.* **2013**, *6*, 38.
(27) Zhou, W.; Yu, Y.; Chen, H.; DiSalvo, F. J.; Abruna, H. D. *J. Am. Chem. Soc.* **2013**, *135*, 16736.
(28) Zhou, W.; Xiao, X.; Cai, M.; Yang, L. *Nano Lett.* **2014**, *14*, 5250.
(29) Peng, H.-J.; Zhang, Q. *Angew. Chem., Int. Ed.* **2015**, *54*, 11018.
(30) Yang, C.-P.; Yin, Y.-X.; Guo, Y.-G.; Wan, L.-J. *J. Am. Chem. Soc.* **2015**, *137*, 2215.
(31) Fan, Q.; Liu, W.; Weng, Z.; Sun, Y.; Wang, H. *J. Am. Chem. Soc.* **2015**, *137*, 12946.
(32) Wang, Y.-X.; Yang, J. P.; Chou, S.-L.; Zhang, R.; Xu, Y.; Fan, J.; Zhang, W.-X.; Liu, H. K.; Zhao, D. Y.; Dou, S. X. *Nano Energy* **2015**, *18*, 133.
(33) Manthiram, A.; Yu, X. W. *Small* **2015**, *11*, 2108.
(34) Chen, S.; Sun, B.; Xie, X.; Mondal, A. K.; Huang, X.; Wang, G. X. *Nano Energy* **2015**, *16*, 268.
(35) Seh, Z. W.; Sun, J.; Sun, Y.; Cui, Y. *ACS Cent. Sci.* **2015**, *1*, 449.